

Constraining accuracy of the pairwise velocities in N -body simulations using scale-free models

Sara Maleubre,^{1,2*} Daniel J. Eisenstein,³ Lehman H. Garrison,^{4,5} and Michael Joyce¹

¹ *Laboratoire de Physique Nucléaire et de Hautes Énergies, UPMC IN2P3 CNRS UMR 7585,*

Sorbonne Université, 4, place Jussieu, 75252 Paris Cedex 05, France

² *Max Planck Institute for Extraterrestrial Physics, Giessenbachstrasse 1, 85748 Garching, Germany*

³ *Center for Astrophysics | Harvard & Smithsonian, 60 Garden St, Cambridge, MA 02138*

⁴ *Center for Computational Astrophysics, Flatiron Institute, 162 Fifth Ave., New York, NY 10010*

⁵ *Scientific Computing Core, Flatiron Institute, 162 Fifth Ave., New York, NY 10010*

Accepted XXX. Received YYY; in original form ZZZ

ABSTRACT

We present a continuation of an analysis that aims to quantify resolution of N -body simulations by exploiting large (up to $N = 4096^3$) simulations of scale-free cosmologies run using ABACUS. Here we focus on radial pairwise velocities of the matter field, both by direct estimation and through the cumulative-2PCF (using the pair conservation equation). We find that convergence at the 1% level of the mean relative pairwise velocity can be demonstrated over a range of scales, evolving from a few times the grid spacing at early times to slightly below this scale at late times. We show the analysis of two different box sizes as well as from averaging results from the smaller boxes, and compare the power of the two aforementioned estimators in constraining accuracy at each scale. Down to scales of order of the smoothing parameter, convergence is obtained at $\sim 5\%$ precision, and shows a behaviour indicating asymptotic stable clustering. We also infer for LCDM simulations conservative estimates on the evolution of the lower cut-off to resolution (at 1% and 5% precision) as a function of redshift.

Key words: cosmology: large-scale structure of the Universe – methods: numerical

1 INTRODUCTION

Observational tests such as Type Ia supernovae (Perlmutter et al. 1997; Riess et al. 1998), large-scale structure analysis from Baryon Acoustic Oscillations (BAO, Eisenstein et al. 2005; Cole et al. 2005) and the temperature anisotropies of the cosmic microwave background (CMB, Jaffe et al. 2001; Pryke et al. 2002; Planck Collaboration et al. 2014) provide compelling evidence that the Universe is in an accelerated expansion. To explain this within the framework of General Relativity requires a new type of “dark” energy that accounts for about 70% of the total, and whose nature is still unknown. In the current standard model of cosmology (LCDM), this energy component is in the form of a cosmological constant. Alternative theoretical approaches either add extra degrees of freedom to characterize the energy content of the Universe or modify the Einstein-Hilbert action (for a review on these models see Clifton et al. 2012).

Ongoing and future surveys such as the Dark Energy Spectroscopic Survey (DESI) (DESI Collaboration et al. 2016) or the space-based mission *Euclid* (Laureijs et al. 2011) will provide large scale structure maps of the Universe of unprecedented statistical precision, allowing astronomers to measure the expansion history of the Universe and the growth rate of cosmic structures in sufficient detail to potentially distinguish between the different possible aforementioned scenarios.

Indeed, one of the most valuable tests to discriminate between

these multiple models observationally, and ultimately determine which can explain current data, consists in the study of the rate at which cosmic structures grow (see e.g. Perenon et al. 2019; Brando et al. 2021), as different theories can predict quite different growth histories even for the same background evolution. A popular way of constraining this growth rate is by analysing the corrections to galaxy redshifts due to their peculiar velocities, which produces a modification of galaxy clustering, an effect called redshift-space distortions (RSD, Jackson 1972; Kaiser 1987). Since peculiar velocities are caused by gravitational pull, we can trace a relation between the velocity field and the mass density field and thus estimate the rate at which structures grow. Countless efforts have been made into modelling these velocities from low-order statistics of the density field (in particular from the 2PCF) (e.g. Mo et al. 1997; Juszkiewicz et al. 1999; Sheth et al. 2001a,b), as well as higher order multiples (Scoccimarro 2004; Shirasaki et al. 2021; Cuesta-Lazaro et al. 2020)

In order to exploit this information, it is essential to calculate accurate theoretical predictions for the large-scale structure of the Universe. Below scales where the perturbative approaches break down, such calculations rely entirely on cosmological simulations performed using the N -body method. This approach approximates the continuous phase-space distribution of dark matter by that of a sparse finite sample of particles, and evolves them in a finite box with periodic boundary conditions. In this context, an important question is the accuracy and scale-range limitations of this method in attaining the physical limit.

* E-mail: sara.maleubre@lphne.in2p3.fr

The assessment of the accuracy to which results converge to values independent of the numerical parameters (time stepping, force accuracy parameters) introduced in the resolution of the N -body system is straightforward. In this respect, extensive code comparisons (Heitmann et al. 2008; Schneider et al. 2016; Garrison et al. 2019; Grove et al. 2022) give considerable added confidence in the precision of results for different statistics. Such comparisons do not address, however, the question of the accuracy with which these simulations represent the physical limit. While dependence on box size can be assessed by direct extrapolation studies (see e.g. Euclid Collaboration et al. 2019), assessing the accuracy limitations imposed at *small scales* due to the discretization of the matter field is much more complex. The reason is that there are, at least, two relevant unphysical parameters, the mean interparticle spacing (denoted Λ here) and the gravitational force smoothing (denoted ϵ), and numerical extrapolation to the continuum physical limit, corresponding to $\epsilon/\Lambda \rightarrow 0$, is in practice unattainable. Precise quantitative conclusions regarding it have remained elusive and sometimes controversial (see Joyce et al. 2021, for a discussion and some references).

Previous studies using N -body simulations have already used the information contained in the dark matter and halo pairwise velocity field to study plausible deviations from the standard model (Hellwing et al. 2014; Gronke et al. 2015; Bibiano & Croton 2017; Hellwing et al. 2017; Dupuy et al. 2019; Valogiannis et al. 2020). Such conclusions ultimately rely on the ability of the N -body method to accurately predict and compute the desired statistic, and that of the chosen halo finder retrieving halo properties accurately. But halos are not uniquely defined entities, and their properties depend strongly on the algorithm adopted for their extraction. We will explore this topic in an accompanying paper (Maleubre et al. 2023).

In this article, we use the techniques introduced in Joyce et al. (2021) and developed and applied also in Leroy et al. (2021); Garrison et al. (2021a); Garrison et al. (2021c) and Maleubre et al. (2022) to derive resolution limits arising from particle discretization for different statistics by analysing deviations from self-similarity in scale-free cosmological models. Here, we employ these methods to assess and quantify the limits arising from discretization on the precision at which the radial component of the pairwise velocity of the full dark matter field can be retrieved from N -body simulations.

This article is structured as follows. The first part of section 2 describes what scale-free cosmologies are and how their self-similar evolution can be used to determine the accuracy at which different statistics can be measured in N -body simulations. Next, we recall the expressions for the radial component of the pairwise velocity and the pair conservation equation, as well as give the equation for the latter in the context of scale-free cosmologies. section 3 contains a summary of the simulations used, as well as a brief description of ABACUS, the N -body code used for their computation. It also contains a description of the method used to estimate convergence of the different statistics in the dark matter field. In section 4 we present and analyse our results, as well as infer resolution limits to non-scale-free cosmologies. Finally, we summarize our main findings in section 5.

2 SCALE-FREE SIMULATIONS AND PAIRWISE VELOCITY

2.1 Scale-free simulations and Self Similarity

Scale-free cosmologies have an Einstein-de Sitter, EdS, ($\Omega_M = 1$) background and a power-law power spectrum ($P_k \propto k^n$) of initial

perturbations, which are thus characterized by just one length scale, the scale of non-linearity. This can be defined by

$$\sigma_{\text{lin}}^2(R_{\text{NL}}, a) = 1 \quad (1)$$

where σ_{lin}^2 is the variance of normalized linear mass fluctuations in a sphere. Its temporal evolution can be calculated from linear perturbation theory as

$$R_{\text{NL}} \propto a^{\frac{2}{3+n}} \quad (2)$$

One can infer that, if the evolution of gravitational clustering is independent of any other length scale (notably ultraviolet or infrared cut-offs to the assumed power-law fluctuations), it must be *self-similar*, i.e., the temporal evolution of the statistics describing clustering is given by a spatial rescaling following Equation 2. More specifically, any dimensionless function $F(x_1, x_2, \dots; a)$ describing clustering (where the x_i are the parameters on which the statistic depends) will obey a relation of the form

$$F(x_1, x_2, \dots; a) = F_0(x_i / X_{\text{NL},i}(a)) \quad (3)$$

where $X_{\text{NL},i}$ encodes the temporal dependence of the characteristic scale with the same dimensions as x_i (as inferred from R_{NL}).

Our interest in self-similarity is driven by the fact that it greatly simplifies the description of clustering: its time dependence is effectively trivial, and any statistic describing clustering is specified by the single time-independent function on the right-hand side of Equation 3. As discussed in our previous papers, we can use this property to determine the range of scales that a simulation can reliably reproduce: any deviation from self-similarity arises necessarily from dependence on the *unphysical scales* proper to the N -body simulations.

2.2 Pairwise Velocity and pair-conservation equation

In this study we focus on the radial component of the mean pairwise velocity defined by

$$v_{12}^r = \left\langle (\mathbf{v}_1 - \mathbf{v}_2) \cdot \frac{\mathbf{r}}{|\mathbf{r}|} \right\rangle \quad (4)$$

where the velocity difference ($\mathbf{v}_1 - \mathbf{v}_2$) of a pair of objects is projected on to their separation vector \mathbf{r} , and $\langle \dots \rangle$ denotes the ensemble average. It can be estimated in a finite simulation by directly averaging the pair velocity over all pairs. To do so, here we have coded an appropriate modification of the analysis tool *Corrfunc* (Sinha & Garrison 2019, 2020). To facilitate our analysis based on self-similarity, we will always consider below the dimensionless ratio of v_{12}^r to the Hubble flow (Hr), so that self-similarity has the simple expression in the form of Equation 3.

This paper focuses on the matter field, and the choice to study v_{12}^r is motivated by the fact that, in this case, it can also be related to the two-point correlations of mass density via the so-called pair conservation equation. This relation was first derived by Davis & Peebles (1977) as a consequence of the BBGKY equations. In their statistical description, matter was approximated by a set of identical particles of mass m , making their theoretical results directly applicable to those of N -body simulations. Starting from the continuity equation for the density contrast (zeroth moment of the Vlasov equation) one obtains the pair conservation equation:

$$\frac{\partial \xi_{12}}{\partial \tau} + \nabla_{12} \cdot [\mathbf{v}_{12}' (1 + \xi_{12})] = 0 \quad (5)$$

where τ is equal to the conformal time and ξ_{12} is the standard reduced two-point density-density correlation function (2PCF) defined as the

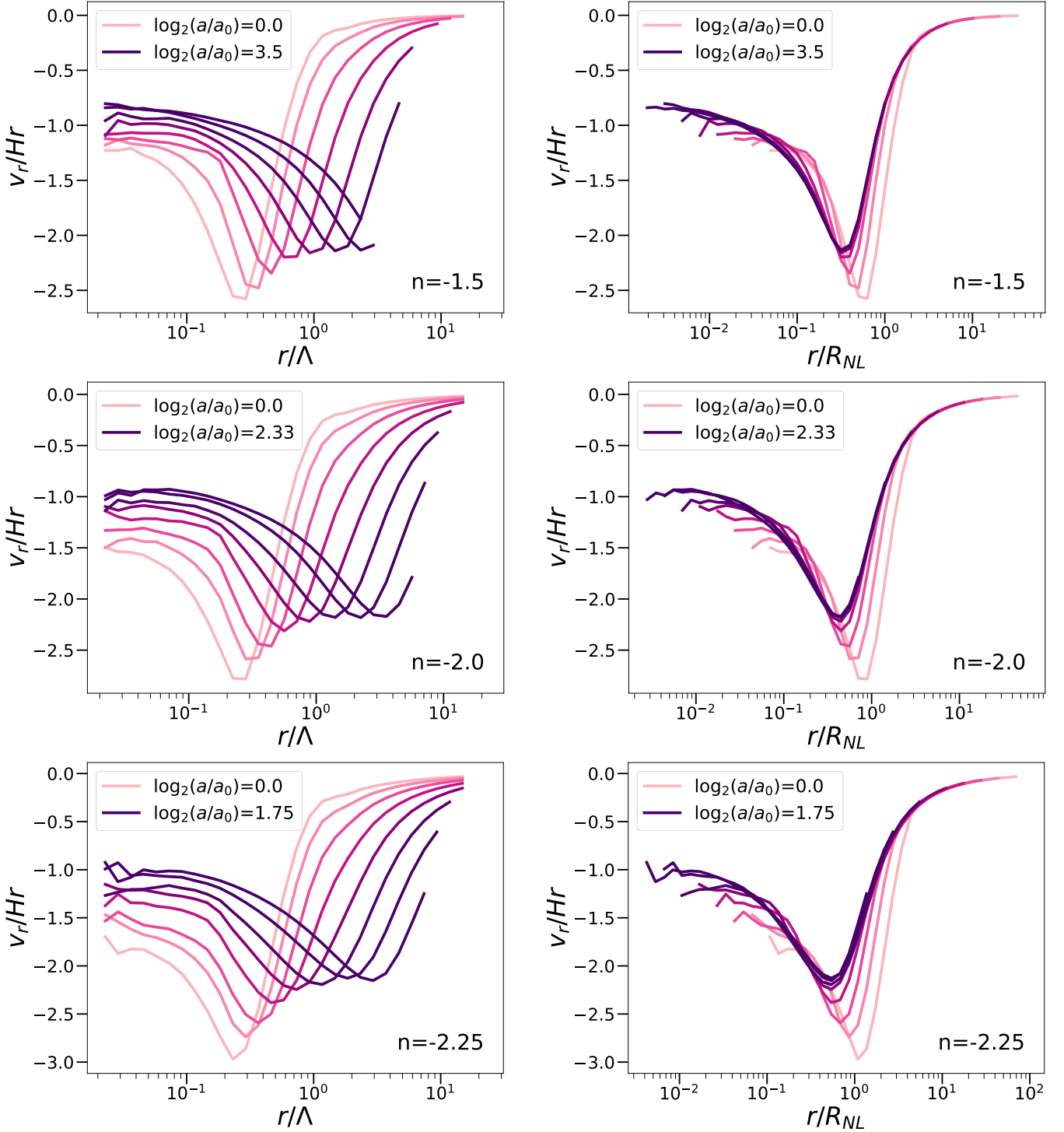


Figure 1. Directly estimated v_r/Hr as a function of comoving separation (left column) and of the rescaled coordinate r/R_{NL} (right column), for simulations with spectral indices $n = -1.5$, $n = -2.0$ and $n = -2.25$ ($N = 4096^3$ for the former exponent and average over four $N = 1024^3$ for the last two). Self-similar evolution corresponds to a superposition of the curves in the rescaled plots. The times shown correspond to every fourth snapshot $S = 0, 4, 8, \dots$ (where S is as defined in Equation 11) over the total time-span of the simulations.

ensemble average at two different locations ($1 + \xi_{12} = \langle (1 + \delta(\mathbf{x}_1))(1 + \delta(\mathbf{x}_2)) \rangle$).

This can be conveniently rewritten as (Nityananda & Padmanabhan

1994):

$$\frac{v_r}{Hr} = -\frac{1}{3(1 + \xi)} \frac{\partial \bar{\xi}}{\partial \ln a} \quad (6)$$

where $\bar{\xi} = 3x^{-3} \int_0^x \xi y^2 dy$, the cumulative two-point correlation function (cumulative 2PCF), is the average 2PCF interior to x where

we have normalized the velocity to the Hubble flow (Hr). For economy, we have dropped the indices 12 in the two-point quantities. As Equation 6 is exact, it implies that we can estimate v_r in a finite sample indirectly, using instead of the velocities themselves the direct estimators of the 2PCF, the cumulative 2PCF and its derivative, combined in the appropriate way. This has been previously exploited in an early study of the pair velocity in scale-free models by Jain (1997) focused on the question of whether clustering become *stable* at small scales (Peebles 1974), i.e. whether it tends to become stationary in physical coordinates, corresponding to $v_r = -Hr$.

In the context of scale-free models and their expected self-similarity, it is convenient to rewrite Equation 6 with the time derivative taken at a fixed value of the rescaled comoving separation (i.e. at fixed r/R_{NL} rather than fixed r)

$$\frac{v_r}{Hr} = -\frac{2}{3+n} \left(\frac{\bar{\xi}}{\xi} - 1 \right) \frac{\xi}{1+\xi} - \frac{1}{3(1+\xi)} \frac{\partial \bar{\xi}}{\partial \ln a} \Big|_{r/R_{\text{NL}}} \quad (7)$$

When the two-point density correlations (as described by ξ and $\bar{\xi}$) are self-similar, the last term vanishes and we can infer that v_r is also self-similar. On the other hand, self-similarity of ξ and $\bar{\xi}$ is not a requirement for that of v_r . We will pay careful attention to this point in our analysis below, and we will show that there is in fact a regime in our simulations in which v_r approximates well self-similarity while the 2PCF does not.

3 NUMERICAL SIMULATIONS

3.1 ABACUS code and simulation parameters

We report results based on the simulations listed in Table 1, performed using the ABACUS N -body code (Garrison et al. 2021b). ABACUS offers high performance and accuracy, based on a high-order multiple method to solve far-field forces and an accelerated GPU calculation of near-field forces by pairwise evaluation. While the $N = 1024^3$ simulations were run using local facilities at the Harvard-Smithsonian Center for Astrophysics (CfA), the larger $N = 4096^3$ simulations are part of the ABACUS SUMMIT project (Maksimova et al. 2021), which used the Summit supercomputer of the Oak Ridge Leadership Computing Facility.

The simulation data we exploit in this article are also summarized in Table 1. As in Maleubre et al. (2022), we have simulated three different exponents ($n = -1.5$, $n = -2.0$ and $n = -2.25$), chosen to probe the range relevant to standard (i.e. LCDM-like) models. For the first two exponents, we have two simulations with different N but otherwise identical parameters, allowing us to study the impact coming from finite box size effects. For the larger ($N = 4096^3$) simulations, the statistics have been calculated on (random) subsamples of different sizes (25%, 3%) to facilitate the assessment of finite sampling effects. For the other two spectral indices, $n = -2.0$ and $n = -2.25$, we have four $N = 1024^3$ simulations, each with identical N -body parameters but different realizations of the IC. These will be analysed below, both individually and as an average, to complement the finite sampling vs. finite box size effects analysis.

Throughout this whole study, we work in units of the mean inter-particle (i.e. initial grid) spacing, $\Lambda = L/N^{1/3}$. The essential time-stepping parameter in ABACUS has been chosen as $\eta = 0.15$ for all simulations, and the additional numerical parameters have been set as detailed in Maleubre et al. (2022) and summarized below. These choices are based on the extensive convergence tests of these parameters reported in our previous studies (see Joyce et al. 2021; Garrison et al. 2021a).

The start of the simulation ($a = a_i$) is chosen so that top-hat density fluctuations at the particle spacing are given by

$$\sigma_i(\Lambda, a_i) = 0.03 \quad (8)$$

while the first output epoch ($a = a_0$)¹ corresponds approximately to the formation of the first non-linear structures, fixed at the time at which fluctuations of peak-height $\nu \approx 3$ are expected to virialize in the spherical collapse model ($\sigma \sim \delta_c/\nu$, with $\delta_c = 1.68$):

$$\sigma_{\text{lin}}(\Lambda, a_0) = 0.56 \quad (9)$$

Subsequent output values are spaced by a factor $\sqrt{2}$ in the non-linear mass scale. Given that $M_{\text{NL}} \propto R_{\text{NL}}^3$ and substituting in Equation 2, we get:

$$\Delta \log_2 a = \frac{3+n}{6} \Delta \log_2 M_{\text{NL}} = \frac{3+n}{12} \quad (10)$$

We use $\log_2(a/a_0)$ as the time variable of our analysis, which indicates how many epochs have passed since the first output. It is also convenient to define the variable

$$S = \frac{12}{3+n} \log_2 \left(\frac{a_S}{a_0} \right) \quad (11)$$

with $S = 0, 1, 2, \dots$ corresponding to the different outputs of the simulation.

With respect to the force softening, as previously described in Garrison et al. (2016), ABACUS uses a spline softening derived using a Taylor expansion to second order in r of a Plummer softening expression, taking the form

$$\mathbf{F}(\mathbf{r}) = \begin{cases} \left[10 - 15 (r/\epsilon_s) + 16 (r/\epsilon_s)^2 \right] \mathbf{r}/\epsilon_s^3, & r < \epsilon_s \\ \mathbf{r}/r^3, & r \geq \epsilon_s \end{cases} \quad (12)$$

which imposes a smooth transition at the softening scale ϵ_s . All softening lengths in this study have been fixed in proper coordinates, decreasing as $\epsilon(a) \propto 1/a$ in comoving coordinates, those used by the simulation. To avoid a too large softening at earlier times, we first fixed it in comoving coordinates down to a_0 , the first output of our simulation, and change it to proper from then on. For all the simulations studied here, we use $\epsilon(a_0)/\Lambda = 0.3$. This value has been chosen following the results in Garrison et al. (2021a) and Maleubre et al. (2022), being both accurate and efficient for the spectral indices analysed.

Initial conditions have been set up using a modification to the standard Zel'dovich approximation (ZA), detailed in Garrison et al. (2016). This includes a second order Lagrangian perturbation theory (2LPT) correction as well as particle linear theory (PLT) corrections as described in Joyce & Marcos (2007) and Garrison et al. (2016). The latter corrects the initial conditions for discreteness effects at early times, so that the result of fluid evolution is reproduced at a target time $a = a_{\text{PLT}}$. For all our simulations here we have $a_{\text{PLT}} = a_0$, with a_0 defined by Equation 9.

3.2 Estimation of converged values

As in our previous papers, we will assess the convergence to the physical limit of a particular statistic by studying its temporal evolution, which becomes time-independent in rescaled variables in the case of self-similarity. To make this study quantitative — i.e. to identify

¹ We emphasize that for this paper a_0 corresponds to the first output of the simulation, and not the scale factor today, as it's usually the case.

Table 1. Summary of the N -body simulation data used for the analysis of this paper. The first column shows the spectral index of the initial PS, N is the number of particles of each simulation, and the third column shows the number of simulations with identical parameters but different realizations of the IC. The fourth column shows the available statistic and sampling of the matter field.

n	N	num. sims.	DM Statistic (%)
$n = -1.5$	4096^3	1	v_r and ξ (25%)
$n = -1.5$	1024^3	1	v_r and ξ (100%)
$n = -2.0$	4096^3	1	ξ (3%)
$n = -2.0$	1024^3	4	v_r and ξ (100%)
$n = -2.25$	1024^3	4	v_r and ξ (100%)

estimated converged values, and converged regions at some precision — we need to adopt appropriate criteria. While the conclusions drawn should not of course depend significantly on the chosen criteria, these criteria are intrinsically somewhat arbitrary in detail. In practice, their choice is made based on visual examination of data. We follow here the simple procedure described in Maleubre et al. (2022). It allows us to estimate a converged value and converged region at a chosen precision, per rescaled bin for each of the statistics analysed in this paper. The method is equivalent for all our matter-field dimensionless statistics (ξ , $\bar{\xi}$, v_r/Hr), and we denote our chosen statistic by X in the following explanation.

Studying temporal self-similar evolution at determined rescaled bins consists in analysing the behaviour of the statistic at vertical slices in the right panels of Figure 1.

We first calculate an estimated converged value (denoted as X_{est}) in each rescaled bin as the average of the statistic in a specific temporal window. The width of this window is conveniently specified by a number of snapshots w , corresponding to an increase in the non-linearity scale by a factor² of $2^{w/6}$ (below we use $w = 5$). To identify which time-window in the span of the whole simulation is the best converged, we “slide” our window of width w across the data to find the one which minimizes

$$\Delta = \frac{|X_{\text{max}} - X_{\text{min}}|}{2\mu_X} \quad (13)$$

where X_{max} , X_{min} , and μ_X are respectively the maximum, minimum, and average values in the window. As a result, X_{est} is a first attempt to calculate the most self-similar value of the requested statistic in a particular rescaled bin. But in reality, we’re only interested in convergence above a particular precision. Specifying now a parameter p characterizing the precision of convergence, any bin is considered to be converged only if the minimal value of Δ is less than p .

As a result, we now know which rescaled bins are converged at a precision p or better, for our studied statistic. Ultimately, we’re interested in identifying the minimum physical scales at which we have access to at any given time. For this, we now need to identify the maximum temporal window behaving self-similarly for each of the converged rescaled bins.

To identify the temporal region of convergence with respect to X_{est} (still at precision p), for each rescaled bin we find the largest (containing at least three consecutive snapshots, though again this number is not essential) connected temporal window verifying

$$\frac{|X - X_{\text{est}}|}{X_{\text{est}}} < p. \quad (14)$$

² Remember that for each subsequent snapshot the non-linearity scale increases by $2^{1/6}$, so the total increase over a time window w will be $2^{w/6}$.

We denote X_{conv} the average calculated over this new largest temporal window, and take this as the final estimated converged value of the statistic for the given rescaled bin. The edges of the window are thus the earliest and latest converged snapshots. We note that, in the following (as in Maleubre et al. 2022), when we say that we have precision at $x\%$ we mean that $p = x/100$ ³.

In the results presented below, all two-point quantities have been calculated over the same r/R_{NL} grid. We use bins of constant logarithmic spacing $1 + (\Delta r/r) \approx 2^{1/12}$ (Maleubre et al. 2022, following), ensuring that bins of different snapshots match when rescaled by R_{NL} to facilitate comparison between them. In order to reduce statistical noise sufficiently, we have rebinned by grouping four such bins, corresponding to $\Delta r/r \approx 0.26$. In our presentation below we label our bins, for simplicity, just by the value of the rescaled variable at the geometrical centre of the bin.

4 RESULTS

As discussed above, in a scale-free cosmology, self-similarity implies an independence of the results of an N -body simulation of their discretization parameters. By carefully examining the departures from self-similarity that are actually measured, we can infer how the resolved scales depend on the unphysical scales in the N -body simulation. We report in this section this analysis for the mean pairwise velocity in the matter field.

4.1 Direct estimation

As discussed in subsection 2.2, v_r/Hr can be estimated directly from the measured particle velocities, or indirectly from measurements of the 2PCF. We consider first the former estimate. Figure 1 shows the estimated v_r/Hr as a function of time (parameterized by the variable $\log_2(a/a_0)$) at different distances, for spectral indices $n = -1.5$, $n = -2.0$ and -2.25 . Each plot correspond to the simulations with the highest number of particles ($N = 4096^3$ for $n = -1.5$, and the average of the four $N = 1024^3$ simulations for the other). The left panel gives v_r/Hr as a function of r/Λ (with Λ the grid spacing), while the right panel gives it as a function of the rescaled variable r/R_{NL} . Self-similarity corresponds to the superposition of the data at different times in the latter plot.

These plots show qualitatively the general behaviour of the statistic, which is similar to that seen for the 2PCF (Joyce et al. 2021) and the PS (Maleubre et al. 2022). Self-similarity can be seen to propagate from larger comoving scales, significantly above Λ at early times, to smaller scales as time evolves. In particular, the scales around the

³ What we denote p here corresponds to $\alpha/2$ in Maleubre et al. (2022).

“turnaround” point — corresponding to the maximal radial infall velocity — are only resolved at later times. As for the 2PCF and PS in our previous studies, the redder the index, the more reduced is the range of approximate self-similarity. This is a reflection primarily of the smaller range of scale-factor which is accessible in simulations of a fixed size as n decreases, and also, as we will see further below, of larger finite box size effects. Finally, we note that all three models appear to show the same behaviour at asymptotically small scales, tending to a value close to -1 , the value predicted by the stable clustering hypothesis. We will assess these behaviours quantitatively below in [subsection 4.3](#).

4.2 Estimation using pair conservation

We next consider the estimation of v_r from the 2PCF, using the exact relation [Equation 7](#) for v_r in terms of ξ , $\bar{\xi}$ and $\dot{\xi}$. As noted, we can also test the validity of the relation when the term in $\dot{\xi}$ vanishes, which corresponds to self-similarity of $\bar{\xi}$. [Figure 2](#) shows the normalized pairwise velocity at each rescaled coordinate for a set of selected redshifts, in the same way as in the right panel of [Figure 1](#). In addition, we have added a dotted line which gives the new estimation obtained using pair conservation. The left panel excludes the non-self-similar term, while the right panel corresponds to the full (exact) expression [Equation 7](#). Finally, each of the small sub-panels shows the scatter between results from direct estimation and pair conservation. To estimate the time derivative, we have simply used a finite difference estimate on the closest two “neighbouring” snapshots.

In the right panels we see that, as required by pair conservation, we recover v_r to a very good approximation from the alternative estimator. The very small differences can be attributed to finite particle number noise and possible systematic offsets due to the discrete estimation of the time derivative. Given the close spacing ([Equation 10](#)) of our snapshots, it is unsurprising that any such effect appears to be small. At small scales, on the other hand, close examination shows that the pair conservation estimator is slightly less noisy than the direct one. This is as might be anticipated: because of the intrinsic dispersion in the pairwise velocities, we can expect its average to have a greater variance than the direct pair count (as noted previously by [Jain 1997](#)). Thus, in assessing what is required to obtain an accurate estimation of the pairwise velocity, one needs to consider between the need to have closely spaced outputs to accurately estimate the time derivative if pair counting is used, or a larger volume for accurate direct estimation.

The left panels, on the other hand, show very large discrepancies between the two estimators, which we can infer as being due to a significant deviation from self-similarity in the corresponding range of the (integrated) 2PCF. Indeed, we can see that this is the case from the corresponding direct analysis of $\bar{\xi}$ displayed in [Figure 3](#): the scales at which the agreement of the estimators break corresponds to the break from self-similarity of $\bar{\xi}$. We note that, at late times, the associated break appears to occur at a scale where v_r/Hr approaches -1 , the value corresponding to stable clustering. Thus, there is indeed a range where approximate self-similarity in v_r appears to persist despite the fact that the 2PCF differ much more from their physical values, and this range appears to correspond, at later times, to that where stable clustering is well approximated.

4.3 Quantitative determination of resolved scales

To better understand, and then also quantify, the limitations on the range of self-similarity arising from the different unphysical simulation parameters (specifically Λ , ϵ and N) we now study more closely

the evolution as a function of time of v_r/Hr (estimated directly and indirectly via pair conservation), and of ξ and $\bar{\xi}$, for fixed values of r/R_{NL} . This corresponds to taking the values on vertical lines in the right panels of [Figure 1](#) (and the equivalent plots for ξ and $\bar{\xi}$). As discussed, self-similarity of the statistic then corresponds to time independence, i.e. to convergence (in some range) of the time series to a fixed value.

[Figure 4](#) and [Figure 5](#), for spectral indices $n = -1.5$ and $n = -2.0$ respectively, shows such plots for three chosen values of r/R_{NL} . (We exclude $n=-2.25$ for economy, but will discuss it further below). To help understand the scales involved in each plot, we also display the values of x/Λ on the upper x -axis. As R_{NL} is a monotonically growing function of time, x/Λ increases from left to right, translating the fact that the spatial resolution relative to the grid increases with time in these plots. We note that in almost all the plots we can identify easily by eye what appears to be a converged value in a finite range of scales (the only exceptions are those of $\bar{\xi}$ in the first panels). In all these cases, a lower cut-off to this converged range is clearly identifiable. As we discussed in the analysis of similar plots in our previous analyses ([Joyce et al. 2021](#); [Maleubre et al. 2022](#)), and will see again in detail now, this lower cut-off clearly corresponds to the resolution limit fixed by the ultraviolet cut-offs (Λ and ϵ).

The different estimators of the statistics shown are indicated in the legend and described in the figure caption. Recall that, as detailed in [Table 1](#), the properties of the simulations analysed differ for the two different exponents. While data for $n = -1.5$ correspond to a single realization of each box size, $n = -2.0$ presents data from four different realizations of $N = 1024^3$ boxes and their statistical average.

In the cases in which the rescaled bin is converged following the criterion specified above in [subsection 3.2](#), at a precision of 1% (i.e. $p = 0.01$), the estimated converged value is indicated as a dashed line and the red shaded region indicates that within 1% of this value. We only plot the converged value of the biggest simulation (for $n=-1.5$) and the one coming from the averaged statistic (for $n=-2.0$), but visual inspection can help assess the convergence of the other boxes, whose converged value needs to coincide. In addition, and to help the reader evaluate the degree of convergence of the different boxes, we add a sub-plot with the dispersion between this converged value and the individual data points from direct estimation coming from *all* our simulations (including the individual $N = 1024^3$ boxes with $n = -2.0$). This value of 1% is chosen because it is approximately the smallest value of p for which we obtain a significant range of contiguous bins satisfying our convergence criteria. It corresponds to the highest precision (i.e. smallest p) at which we can in practice establish convergence using our data.

The first panel of each figure corresponds to a highly non-linear (small) scale. Although v_r/Hr is not converged at the 1% precision level, the different estimators nevertheless give highly consistent values and appear to show robust convergence albeit at lower precision (of order a few percent), starting from a scale well below Λ . As anticipated in the previous section, the converged value is close to -1 . Further, we see more clearly that this convergence is indeed not associated with that of $\bar{\xi}$, i.e. at this scale the measured *cumulative* 2PCF $\bar{\xi}$ approximates very poorly its physical value.

The next (second) set of panels (of both [Figure 4](#) and [Figure 5](#)) corresponds to the bin around the smallest rescaled separation for which v_r/Hr (in the statistically largest available simulation, using direct estimation) converges (according to our convergence criterion, at the chosen 1% precision level). The lower cut-off to the convergence of v_r/Hr is just slightly below the grid spacing (at about $\Lambda/2$). We see also that $\bar{\xi}$ shows convergence starting from the same scale, so the

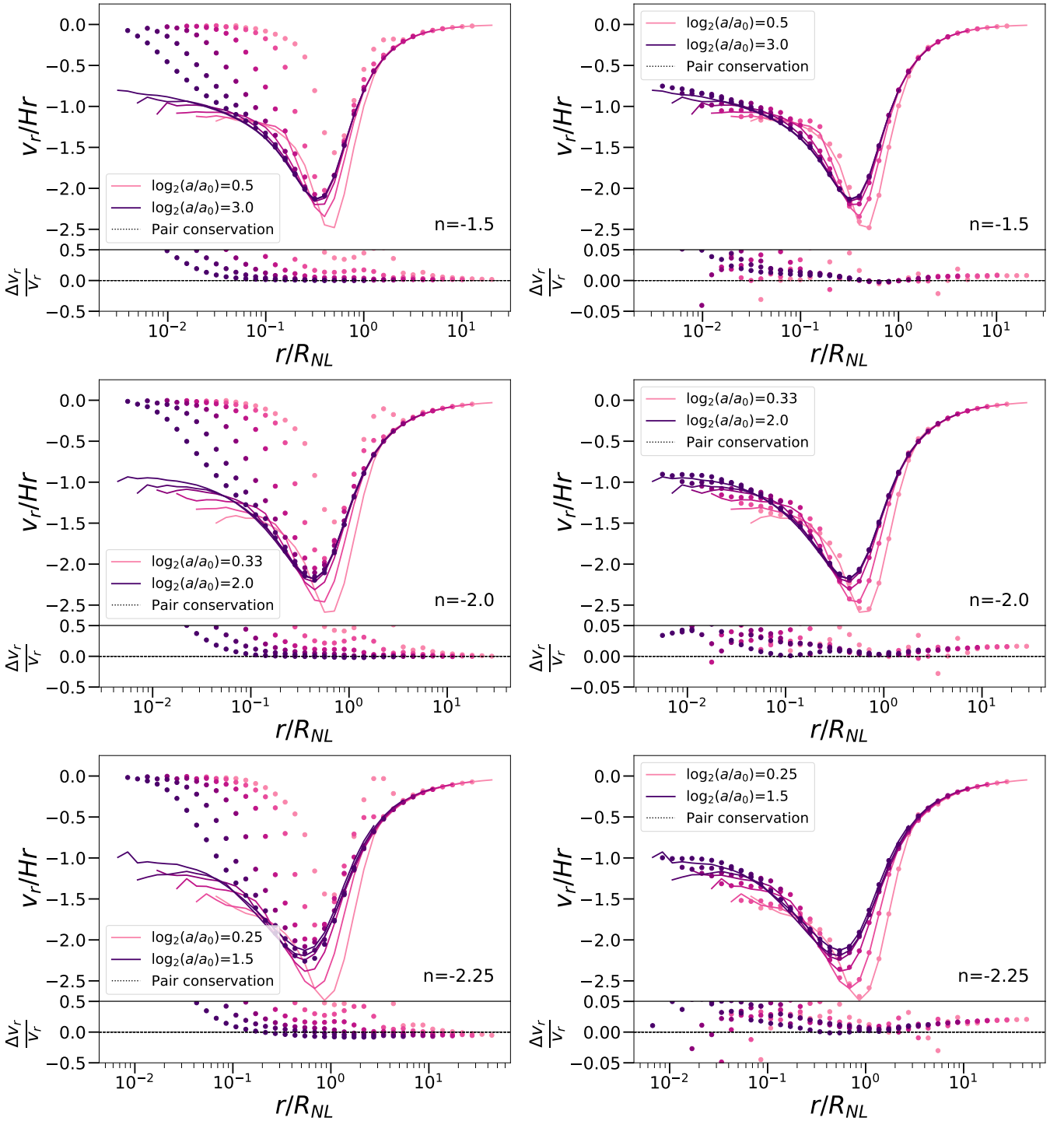


Figure 2. Comparison of different estimators of v_r/Hr as a function of the rescaled length r/R_{NL} , for the same simulations as in Figure 1. The solid lines in each pair of panels (left and right) are identical and correspond to the results obtained by direct estimation using the velocities (as in Figure 1). The dots correspond, in the left panels, to estimations using pair-counting and the assumption of self-similarity of the 2-pt statistics i.e. using Equation 7 with the last term set to zero. In the right panels, this last term is also included in the estimator. The bottom section of each panel shows the difference between pair conservation estimation and direct estimation, with respect to the latter. Note that the y-axis scale has been reduced by $\times 10$ from the left to the right panels.

range of convergence for the pair counting estimator using $\xi^{\dot{}} = 0$, i.e. assuming self-similarity of $\xi^{\dot{}}$, will be accurate in a similar range. Looking at the lower sub-panels in the plots of v_r/Hr , we see that the convergence of the direct estimators in the individual $N = 1024^3$ simulations is degraded just above Λ for $n = -1.5$ and slightly below

for $n = -2.0$. This is simply finite N noise in the estimators, as the associated fluctuations disappear in the larger ($N = 4096^3$) simulation for $n = -1.5$ but also when the four $N = 1024^3$ simulations are combined for $n = -2$ (thus ruling out finite boxsize as the origin of these differences).

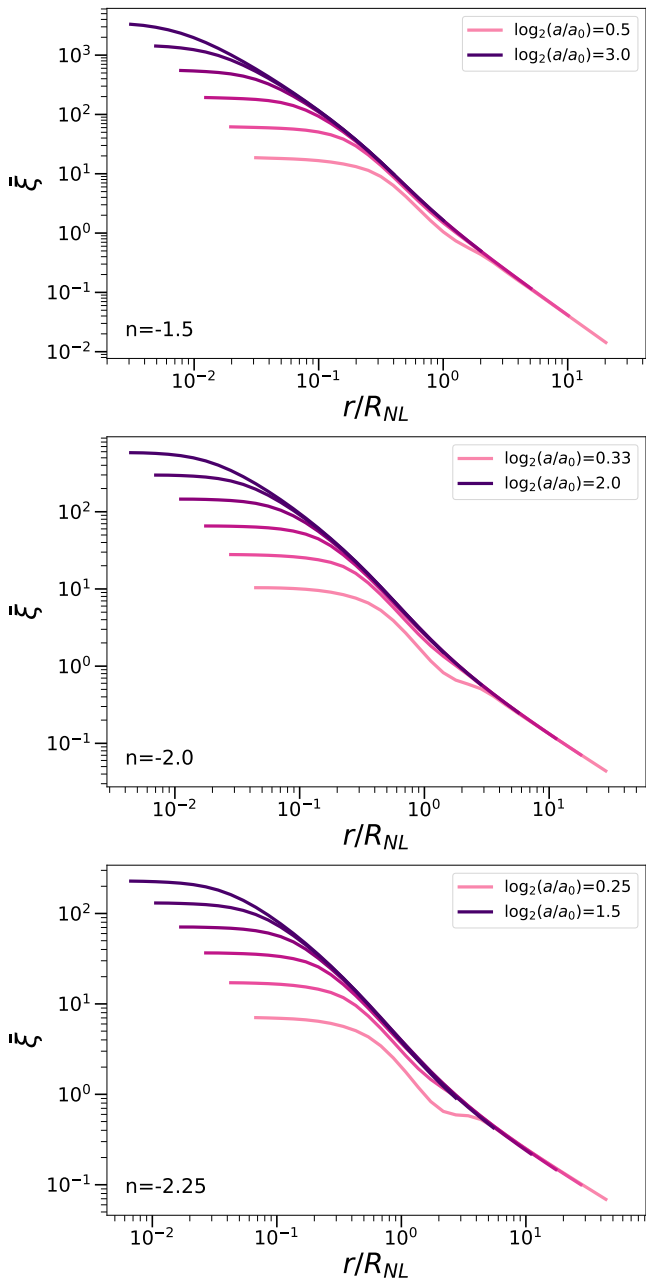


Figure 3. Cumulative 2PCF as a function of rescaled length r/R_{NL} at same times as in Figure 2. Simulations correspond to $n = -1.5$, $n = -2.0$ and $n = -2.25$, with $N = 4096^3$ in the former exponent and the average over four $N = 1024^3$ for the other two.

The third row of both figures shows a considerably larger scale, in the weakly non-linear regime, which have a lower cut-off to convergence (again, at the 1% level) a few times larger than the grid spacing. In this case, for $n = -1.5$, there is no visible evidence for the finite N effects seen in the previous bin. On the contrary, for $n = -2.0$, we observe much poorer convergence of v_r/Hr , both in the direct estimations (symbols) and in the pair counting estimator (solid lines in main panel), and it is visible whether we look at the individual simulations or the average statistic. Further, we see now an offset from the estimated converged value that is a systematic shift rather than a random noise, and even in the average over the four simulations. Thus, we can detect a break from convergence within the range

of scales probed. The cancellation (or at least partial cancellation) of these systematic offsets when the realizations are averaged indicates that, at intermediate scales, this is due to significant differences in the initial power at larger scales due to the finite sampling of modes. On the other hand, the observed break from convergence at larger scales (in the average) can be attributed to finite box size effects arising from the missing power in modes below the fundamental of the simulation box, finite L , and no longer due to a finite N as before. These same tendencies are present, but even much more pronounced for $n = -2.25$ (data not shown). Indeed, in this case, the lower and upper cut-offs to convergence below the few percent level are no longer clearly separable from one another in almost all bins. For this reason, we do not use the $n = -2.25$ below in our quantitative assessment of resolution limits.

Summarizing, we can state that:

- At any given converged scale, direct estimation and *full* pair conservation estimation (using the whole expression in Equation 7) of v_r give equivalent results.
- The direct estimation of v_r is more affected by finite N noise than the pair conservation estimation. This is a direct result of the larger variance of v_r with respect to the 2PCF.
- The v_r statistic is more affected by finite boxsize effects (small L) than the 2PCF. Thus, we can observe deviations from self-similarity at smaller scales in the former statistic than in the latter.

4.4 Resolution as a function of time

Applying the analysis detailed above to all bins, we can deduce the comoving scales that are resolved (i.e. self-similar) at each given time, for each of the statistics and estimators we have calculated.

Figure 6 shows the comoving separation, in units of the grid spacing, of the resolved bins at the 1% (upper two panels) and 5% (lower two panels) precision levels, i.e. of the bins found to be converged according to the criteria described in subsection 3.2 for $p = 0.01$ and $p = 0.05$. The points in the left panels are for the mean pairwise velocity direct estimate using the $N = 4096^3$ simulation for $n = -1.5$ and the average over the four $N = 1024^3$ simulations for $n = -2$. The right panels show the *cumulative* 2PCF using the same simulations.

The resolution ranges for ξ^{\ddagger} (in the right panels) can be taken essentially to be those for the mean pairwise velocity estimated from pair conservation and imposing the additional constraint that ξ^{\ddagger} is resolved, i.e. $\xi^{\ddagger} = 0$, because $\xi(r)$ is always resolved starting from a significantly smaller scale than for ξ^{\ddagger} as can be seen in the right panels of Figure 4 and Figure 5. This is just a simple consequence of the fact that ξ^{\ddagger} , by definition, is sensitive (at any given precision level) to $\xi(r)$ over a range of scale below r . It will only therefore be resolved starting from a lower cut-off, below which $\xi(r)$ is resolved over some significant range.

Comparing the upper panels, we see that the scales at which v_r is resolved from direct estimation (left panel) and would be from a *reduced* pair conservation estimation (imposing $\xi^{\ddagger} = 0$) are very similar. A relaxation of the self-similarity constraint in the *cumulative* 2PCF would extend only very modestly the resolved regions, and only at very late times, at least for the case of convergence at the 1% level. There are some additional bins that meet the convergence criterion for the direct estimator, but most of them are not contiguous with the main converged region and thus do not actually extend the lower limit to resolution (i.e. the scale below which convergence is affected by the unphysical UV scales).

In contrast, at 5% precision (lower panels), there is a very marked

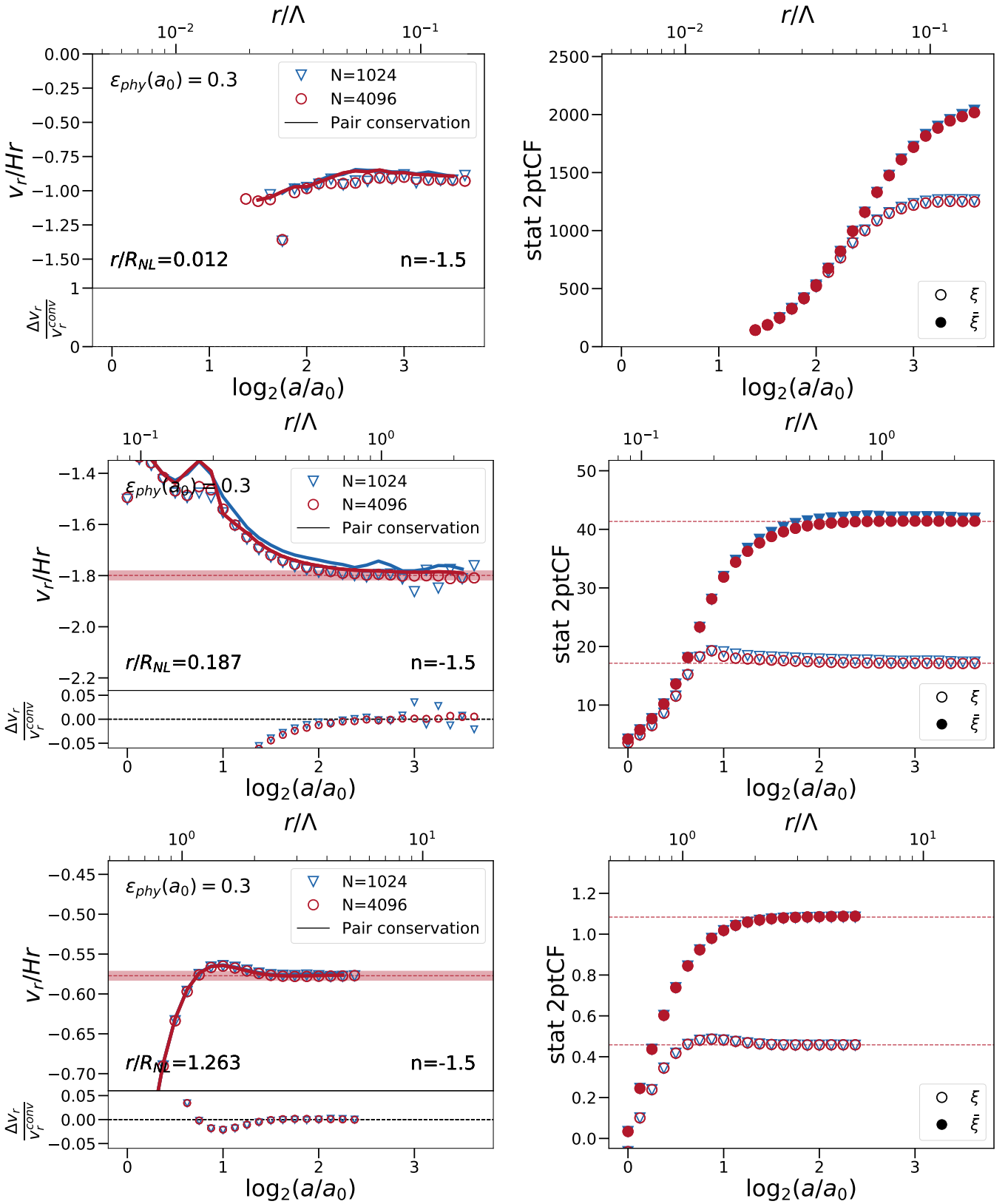


Figure 4. Evolution, for $n = -1.5$ simulations, of v_r/Hr (left panels), and of the 2PCF and *cumulative* 2PCF (right panels), as a function of logarithmic scale factor $\log_2(a/a_0)$, lower x-axis, and as a function of r/Λ , upper x-axis. Each row correspond to a different bin of rescaled separation r/R_{NL} as labelled. The blue triangular symbol represents the smaller $N = 1024^3$ simulation, while the red circles represent the $N = 4096^3$ simulation. Results obtained using the pair counting estimator are drawn as a continuous line in the appropriate colours. Horizontal red dashed lines indicate the converged value of each of the three statistics, calculated from the largest simulation as described in the text, and the red shaded region indicates that within $\pm 1\%$ of this value. The sub-panels in the plots of v_r/Hr give the dispersion of the results obtained using the direct estimation with respect to the converged value.

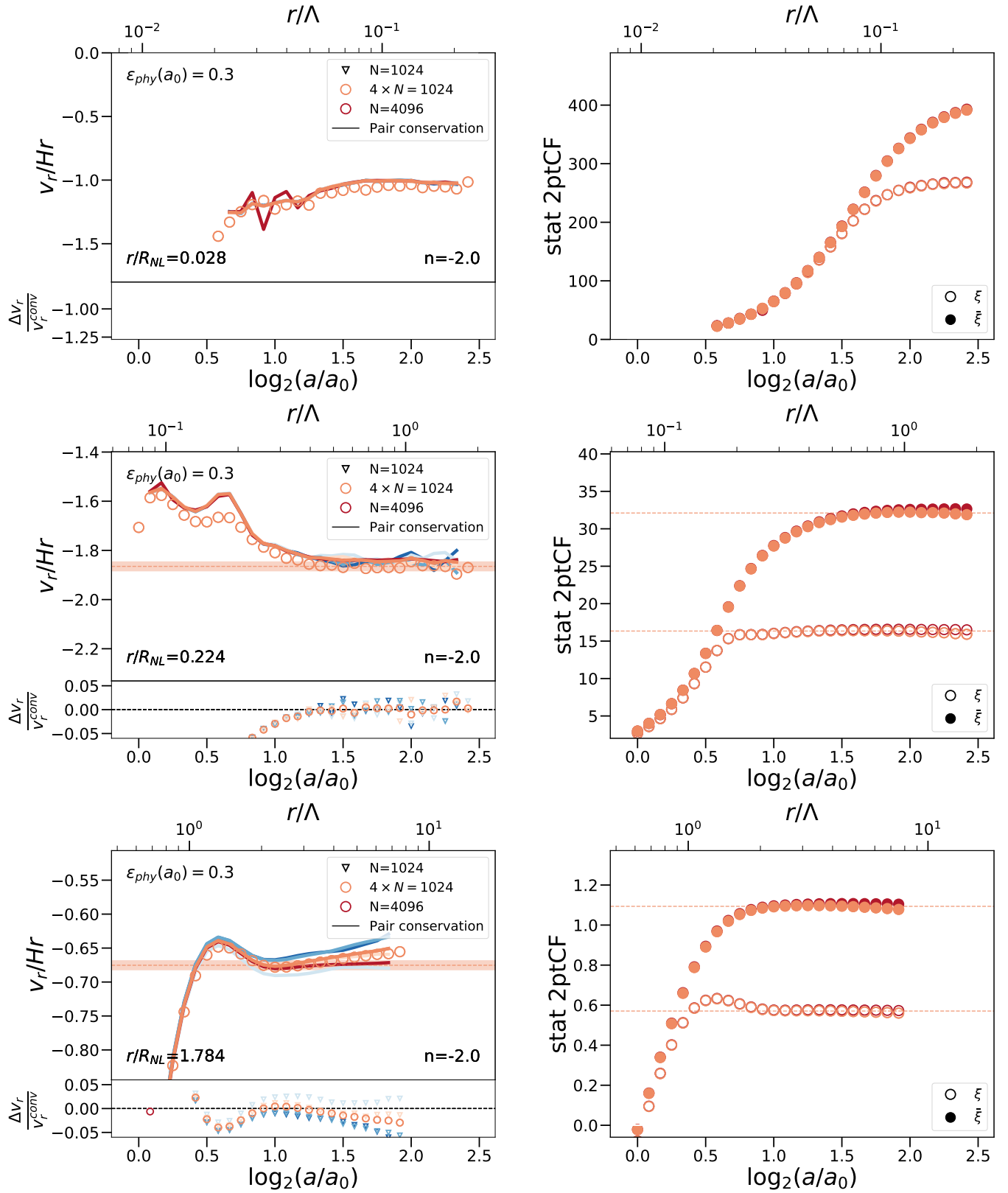


Figure 5. Same as Figure 4, but for $n = -2.0$ simulations. There are now four sets of triangular symbols representing the different $N = 1024^3$ simulations (in the sub-panels only), while the orange circles represent the average of the four. Note further that the results for v_r/Hr from the $N = 4096^3$ simulation are all obtained by pair counting only, so that there are no red circles in the left panels.

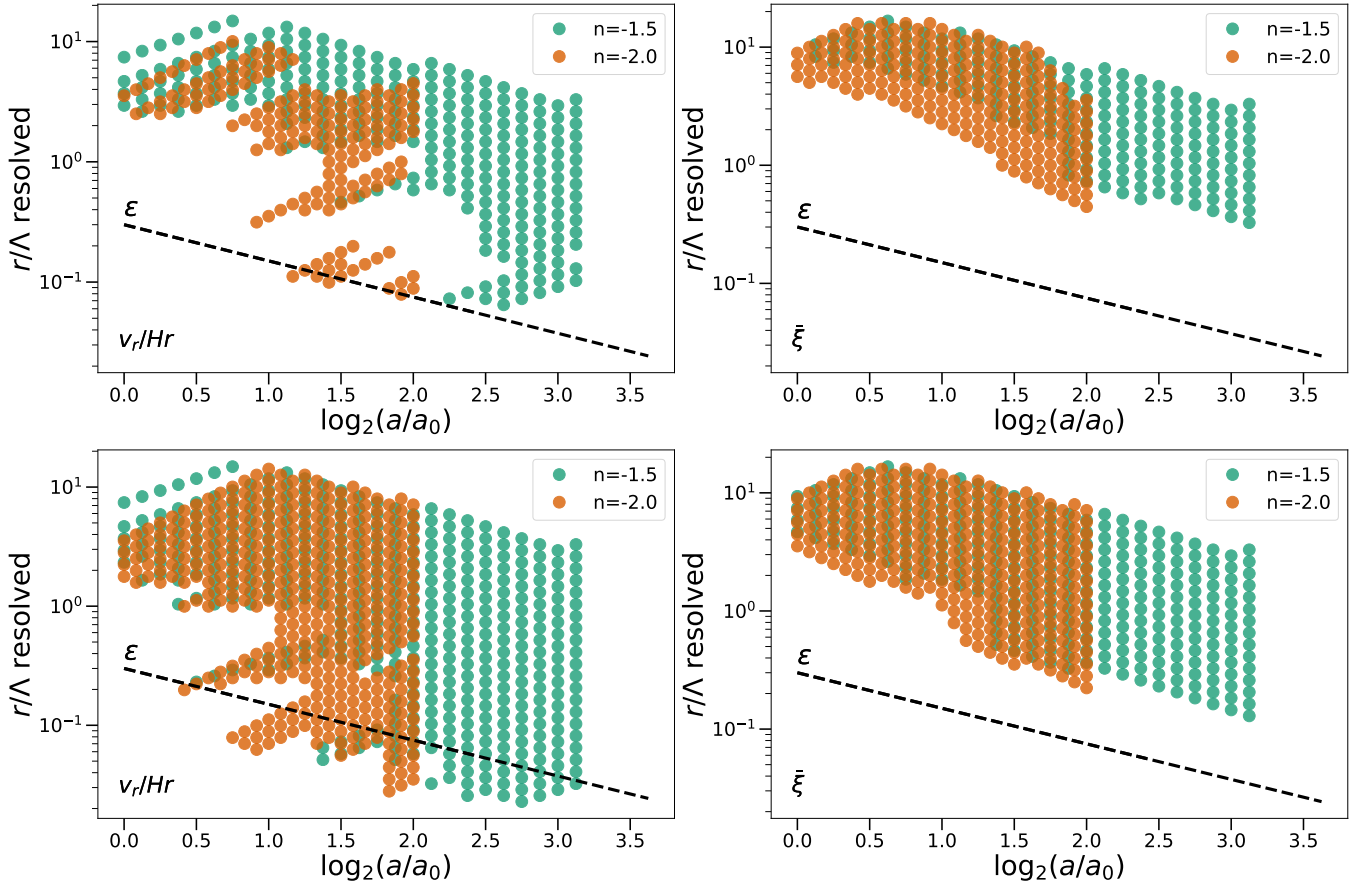


Figure 6. Resolved scales (in units of the initial grid-size, Λ) at 1% (upper row) and 5% (lower row) precision as a function of $\log_2(a/a_0)$. We show results for the spectral indices $n = -1.5$ and $n = -2.0$ (in green and orange, respectively) using the simulations with $N = 4096^3$ for the former and the average of four $N = 1024^3$ simulations for the latter. The left panels show the results for v_r/Hr (direct estimation), while the right shows the results for the *cumulative* 2PCF. The black dashed line shows the evolution of the softening-length ϵ in units of Λ (which is the same in all simulations).

difference between the two plots: as anticipated from our more qualitative analysis above, we see that the resolution of the pairwise velocity now extends down to scales of order the softening length (indicated by the dashed line in each plot). As we will discuss further below, the apparent explanation for this is that the behaviour of the pairwise velocity at these small scales — corresponding to stable clustering — remains the same whether the spatial clustering is resolved or not.

4.5 Resolution limits extrapolated to LCDM

LCDM models are not scale-free: the linear PS is not a power-law, and there are deviations from EdS power-law scale factor. Nevertheless, the latter deviations are only at very low redshift and the PS, in the range of scales relevant to large scale structure formation in cosmology, can be well approximated as a slowly varying power-law: its logarithmic slope varies roughly between $n = -2.5$ and $n = -1.5$ over two decades in scale. From Figure 6 we see that the behaviour of the lower cut-off to resolution is quite weakly dependent on n when plotted as a function of a/a_0 . Thus, we can confidently bracket the lower resolution limits (due to the *UV* cut-offs, Λ and ϵ) using the scale-free results.

As discussed in our previous analyses (a summary of the relevant information can be found in appendix A), for a given physical grid spacing of a LCDM simulation, one can infer a_0 and then obtain a

conversion between redshift z and the variable $\log_2(a/a_0)$, which allows an approximate “mapping” of the scale-free results to the LCDM simulation. Taking the tighter bounds obtained for $n = -1.5$, Figure 7 shows an example of conservative resolution for a simulation with $\Lambda = 0.5h^{-1}\text{Mpc}$. Results are given for a 1% (orange) and 5% (blue) precision in the direct estimation of the pairwise velocity, as plotted in the left panels of Figure 6. Note that the larger missing scales at 5% simply show that v_r/Hr is converged at much earlier redshifts.

4.6 Converged mean pairwise velocities and stable clustering

Having focused on identifying the resolved scales, it is also interesting to look at what can be inferred about the behaviour of the studied statistics, and in particular about their behaviour at asymptotically small scales, where the convergence or deviation from stable clustering is of particular interest.

We show in Figure 8 the converged values of the normalized pairwise velocity for the three simulated spatial indices. These values correspond to the same analysis used to obtain the left panels in Figure 6, but while these show the resolved regions, we now plot the corresponding converged values in each rescaled bin determined by this analysis (i.e. the mean values X_{conv} from the discussion in subsection 3.2). The points plotted are a combination of the values for the bins converged at the 1% level and at the 5% level: we plot

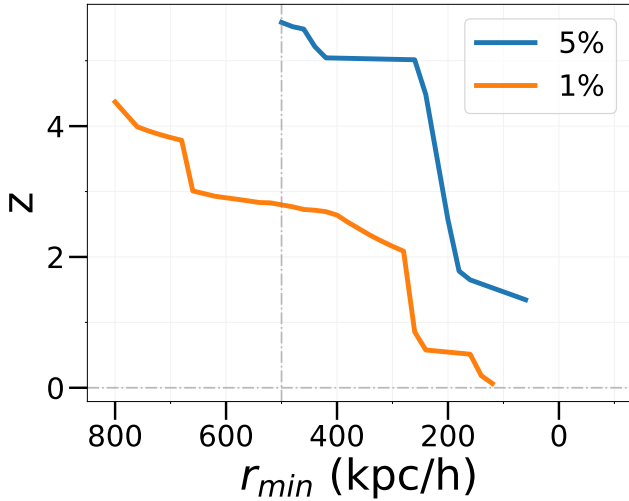


Figure 7. Minimum comoving scale r_{\min} at which v_r/Hr is resolved as a function of redshift, estimated for a standard LCDM cosmology (“Planck 2013”, [Planck Collaboration et al. \(2014\)](#)) in an N -body simulation with a mean-interparticle spacing of $0.5h^{-1}$ Mpc (indicated by dashed vertical line). The orange (blue) line corresponds to the 1% (5%) precision limits, calculated using data from direct estimation as displayed in the left panels of [Figure 6](#), for the $N = 4096^3$ with $n = -1.5$ simulation.

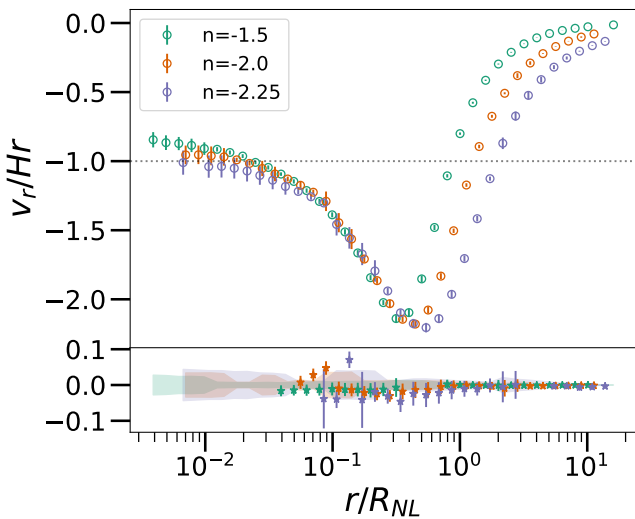


Figure 8. Estimated converged v_r/Hr as a function of rescaled separation, for the three different indicated exponents. In the main plot the same data has been used for the left panels in [Figure 6](#) i.e. using direct estimation. The converged values are obtained using the 1% and 5% precision criteria, with the error bars estimated as described in the text. The sub-plot shows these same errors as shaded regions; it also shows (star symbols) the relative difference with the converged values obtained using pair counting estimation.

X_{conv} for all bins converging at $p = 0.01$, and then also for the bins which do not converge at $p = 0.01$ but do at $p = 0.05$. We add an indicative estimate of the error on X_{conv} which takes into account the expectation that it will decrease as the size of the converged window increases:

$$\delta = \pm p \sqrt{\frac{w_{\min}}{w}} \quad (15)$$

where w is the size (in consecutive snapshots) of the converged

window (used to calculate X_{conv}) and w_{\min} the smallest window for which [Equation 14](#) is satisfied (we have taken here $w_{\min} = 3$). Error bars for the 1% level are smaller than the points, thus where the error bars are visible, the corresponding bins converge only at the 5% level. As could be anticipated, we see that both the accuracy and range of scale measured increases as n does.

We see in this plot that, while there is a clear n -dependence in the shape of the function at larger scales, the behaviour at asymptotically small scales shows a remarkable consistency towards a “universal” stable clustering (bearing in mind that the error bars are only quite rough estimates of the systematic uncertainties due to finite resolution). Positing this to be the correct physical limit also explains why it can be measured quite well even at scales where the physical behaviour of the clustering is not itself resolved: stable clustering is a robust behaviour that it is not spoiled by the discretization of the density field in an N -body simulation.

5 CONCLUSIONS

The analysis we have reported here is an extension of that in a set of papers [Joyce et al. \(2021\)](#); [Leroy et al. \(2021\)](#); [Garrison et al. \(2021a\)](#); [Garrison et al. \(2021c\)](#); [Maleubre et al. \(2022\)](#), which have shown the usefulness of self-similarity and scale-free cosmologies in quantifying resolution of cosmological N -body simulations. Our focus here has been on the radial component of the pairwise velocity in the full matter field. We have also extended, as a complement and for comparison, the analysis of the 2PCF of the matter field (previously studied in [Joyce et al. \(2021\)](#); [Garrison et al. \(2021a\)](#)). Compared to these previous studies which used a single power law ($n = -2.0$) and simulations of a single size ($N = 1024^3$), as in [Maleubre et al. \(2022\)](#) we have considered a set of both different power laws and different box sizes. Unsurprisingly, we have found that the same methods indeed allow us to quantify the evolution of resolution at small scales of the mean pairwise velocity, and further confirm the high levels of accuracy attained by the `ABACUS` code, also in its determination of correlations in the velocity field.

Our exploitation here of simulations of different sizes, of several IC realizations, and of scale-free models with different exponents has allowed us not only to improve some of the results in previous work but has also been essential to allow us to extend the method to a velocity statistic. This is the case because it is crucial for an accurate determination of the precision of convergence to be able to separate very clearly the effects of discretization at small scale from both the noise and systematic effects at large scales due to the finite box size. For the pairwise velocity statistics, which are more sensitive than the 2PCF to these effects, the comparison of different (and larger) box sizes and different exponents turns out to be essential to disentangle clearly the different effects. We have also exploited the two different estimators of the velocity statistic — directly from the particles’ velocities in the simulation or indirectly by pair-counting — to identify noise due to finite size effects. The comparison of different exponents has allowed us also to see how the range of converged scales markedly degrades due to finite size effects as n decreases, and in practice our $n = -2.25$ simulations are not useful for placing precision limits at the 1% level. Further, we argue that our results for the evolution of small scale resolution can be extrapolated to LCDM type models, as they are, when suitably expressed, very weakly dependent on scale-free index n (which values have been chosen to probe the relevant range in LCDM). The same is not true of box size effects, which are strongly n dependent, and indeed we do not attempt to make an extrapolation for these.

We have found that we can determine the evolution of lower cut-off to resolution at the 1% level for the radial pairwise velocity. In addition, we show that it is approximately equal to the corresponding cut-off for the *cumulative* 2PCF, which converges at the same precision level varying from a few times the grid spacing at early times to slightly below this scale at late times. This is a few times larger than the scale at which the 2PCF itself attains the same precision [Joyce et al. \(2021\)](#); [Garrison et al. \(2021a\)](#). This reflects the coupling of the velocity correlation at a given scale to the clustering at smaller scales (as expressed through the integral $\bar{\xi}$ in the self-similar limit).

On the other hand, at 5% precision we have obtained resolution extending down to scales of order the softening length, ϵ , where even the 2PCF is far from its converged value [Joyce et al. \(2021\)](#); [Garrison et al. \(2021a\)](#). In the corresponding range of scale $v_r/Hr \approx -1$, i.e. the result is consistent with the so-called stable clustering hypothesis in which non-linear structures become stationary in physical coordinates [Peebles \(1974\)](#). The conclusion that clustering may indeed tend to this behaviour at asymptotically small scales is consistent with an early analysis (with much smaller simulations, $N \sim 10^6$) of the question using pairwise velocities by [Jain \(1997\)](#) (estimated by pair-counting), and also with results for the shape of the power spectrum at large k reported in [Maleubre et al. \(2022\)](#). In this hypothesis, the fact that resolution extends to such small scales for v_r/Hr is simply due to the fact that the stable behaviour is not spoiled by the discretization of the matter field, and persists even if the clustering is very different to that in the continuum model.

With respect to the preparation of theoretical predictions for forthcoming surveys, and specifically for redshift space distortions, our analysis of the pairwise velocity gives only an indication of the resolution limits at small scales in N -body simulations. It would be straightforward to extend our analysis to additional statistics used in this context, e.g. PDFs of the pairwise velocity and their moments (see references in introduction). Further, to attain a quantification of bounds for the typically cited target 1% level would require slightly more data sets than what we have used here — either slightly larger simulations, or a couple of realizations of the same size as our largest simulations here.

We conclude with some comments on other possible further developments of this work. Our analysis of the mean pairwise velocities in the dark matter field (cf. [Figure 8](#)) shows an apparently universal shape below the scale of maximal infall, and going asymptotically to stable clustering. It would be interesting to compare these results with those in LCDM, making use of the resolution limits we have determined here, to assess whether we indeed find the same behaviour. To establish the evidence for stable clustering at asymptotically small scales, a fuller comparative joint analysis of the 2PCF, PS, and pairwise velocity itself should be performed.

ACKNOWLEDGEMENTS

S.M. thanks the Institute for Theory and Computation (ITC) and the Flatiron Institute for hosting her in early 2022, and acknowledges the Fondation CFM pour la Recherche and the German Academic Exchange Service (DAAD) for financial support. S.M. and M.J. thank Pauline Zarrouk for useful discussions.

D.J.E. is supported by U.S. Department of Energy grant, now DE-SC0007881, NASA ROSES grant 12-EUCLID12-0004, and as a Simons Foundation Investigator.

This research used resources of the Oak Ridge Leadership Computing Facility at the Oak Ridge National Laboratory, which is supported by the Office of Science of the U.S. Department of Energy un-

der Contract No. DE-AC05-00OR22725. The ABACUSSUMMIT simulations have been supported by OLCF projects AST135 and AST145, the latter through the U.S. Department of Energy ALCC program.

DATA AVAILABILITY

Data access for the simulations part of ABACUSSUMMIT is available through OLCF's Constellation portal. The persistent DOI describing the data release is [10.13139/OLCF/1811689](https://doi.org/10.13139/OLCF/1811689). Instructions for accessing the data are given at <https://abacussummit.readthedocs.io/en/latest/data-access.html>.

Data corresponding to the smaller simulations as well as the derived data generated in this research will be shared on reasonable request to the corresponding author.

REFERENCES

- Bibiano A., Croton D. J., 2017, *MNRAS*, **467**, 1386
 Brando G., Koyama K., Wands D., 2021, *JCAP*, 2021, 013
 Clifton T., Ferreira P. G., Padilla A., Skordis C., 2012, *Physics Reports*, **513**, 1
 Cole S., et al., 2005, *MNRAS*, **362**, 505
 Cuesta-Lazaro C., Li B., Eggemeier A., Zarrouk P., Baugh C. M., Nishimichi T., Takada M., 2020, *Monthly Notices of the Royal Astronomical Society*, **498**, 1175
 DESI Collaboration et al., 2016, arXiv e-prints, p. [arXiv:1611.00036](https://arxiv.org/abs/1611.00036)
 Davis M., Peebles P. J. E., 1977, *ApJS*, **34**, 425
 Dupuy A., Courtois H. M., Kubik B., 2019, *MNRAS*, **486**, 440
 Eisenstein D. J., et al., 2005, *ApJ*, **633**, 560
 Euclid Collaboration et al., 2019, *MNRAS*, **484**, 5509
 Garrison L. H., Eisenstein D. J., Ferrer D., Metchnik M. V., Pinto P. A., 2016, *MNRAS*, **461**, 4125
 Garrison L. H., Eisenstein D. J., Pinto P. A., 2019, *MNRAS*, **485**, 3370
 Garrison L. H., Joyce M., Eisenstein D. J., 2021a, *MNRAS*, **504**, 3550
 Garrison L. H., Eisenstein D. J., Ferrer D., Maksimova N. A., Pinto P. A., 2021b, *MNRAS*, **508**, 575
 Garrison L. H., Abel T., Eisenstein D. J., 2021c, *MNRAS*, **509**, 2281
 Gronke M., Llinares C., Mota D. F., Winther H. A., 2015, *MNRAS*, **449**, 2837
 Grove C., et al., 2022, *MNRAS*, **515**, 1854
 Heitmann K., et al., 2008, *Computational Science and Discovery*, **1**, 015003
 Hellwing W. A., Barreira A., Frenk C. S., Li B., Cole S., 2014, *Phys. Rev. Lett.*, **112**, 221102
 Hellwing W. A., Nusser A., Feix M., Bilicki M., 2017, *MNRAS*, **467**, 2787
 Jackson J. C., 1972, *MNRAS*, **156**, 1P
 Jaffe A. H., et al., 2001, *Phys. Rev. Lett.*, **86**, 3475
 Jain B., 1997, *MNRAS*, **287**, 687
 Joyce M., Marcos B., 2007, *Phys. Rev. D*, **76**, 103505
 Joyce M., Garrison L., Eisenstein D., 2021, *MNRAS*, **501**, 5051
 Juszkiewicz R., Springel V., Durrer R., 1999, *ApJ*, **518**, L25
 Kaiser N., 1987, *MNRAS*, **227**, 1
 Laureijs R., et al., 2011, arXiv e-prints, p. [arXiv:1110.3193](https://arxiv.org/abs/1110.3193)
 Leroy M., Garrison L., Eisenstein D., Joyce M., Maleubre S., 2021, *MNRAS*, **501**, 5064
 Maksimova N. A., Garrison L. H., Eisenstein D. J., Hadzhiyska B., Bose S., Satterthwaite T. P., 2021, *MNRAS*, **508**, 4017
 Maleubre S., Eisenstein D., Garrison L. H., Joyce M., 2022, *MNRAS*, **512**, 1829
 Maleubre S., Eisenstein D. J., Garrison L. H., Joyce M., 2023, arXiv e-prints, p. [arXiv:2308.00438](https://arxiv.org/abs/2308.00438)
 Mo H. J., Jing Y. P., Borner G., 1997, *MNRAS*, **286**, 979
 Nityananda R., Padmanabhan T., 1994, *MNRAS*, **271**, 976
 Peebles P. J. E., 1974, *ApJ*, **189**, L51

- Perenon L., Bel J., Maartens R., de la Cruz-Dombriz A., 2019, *JCAP*, 2019, 020
- Perlmutter S., et al., 1997, *ApJ*, 483, 565
- Planck Collaboration et al., 2014, *A&A*, 571, A16
- Pryke C., Halverson N. W., Leitch E. M., Kovac J., Carlstrom J. E., Holzzapfel W. L., Dragovan M., 2002, *ApJ*, 568, 46
- Riess A. G., et al., 1998, *The Astronomical Journal*, 116, 1009
- Schneider A., et al., 2016, *JCAP*, 2016, 047
- Scoccimarro R., 2004, *Phys. Rev. D*, 70, 083007
- Sheth R. K., Hui L., Diaferio A., Scoccimarro R., 2001a, *MNRAS*, 325, 1288
- Sheth R. K., Diaferio A., Hui L., Scoccimarro R., 2001b, *MNRAS*, 326, 463
- Shirasaki M., Huff E. M., Markovic K., Rhodes J. D., 2021, *ApJ*, 907, 38
- Sinha M., Garrison L. H., 2019, in Majumdar A., Arora R., eds, Software Challenges to Exascale Computing. Springer Singapore, Singapore, pp 3–20, https://doi.org/10.1007/978-981-13-7729-7_1
- Sinha M., Garrison L. H., 2020, *MNRAS*, 491, 3022
- Valogiannis G., Bean R., Aviles A., 2020, *JCAP*, 2020, 055

APPENDIX A: MAPPING FROM EDS TO LCDM-LIKE COSMOLOGIES

Following the steps of our previous studies using scale-free simulations, we have characterized how resolution depends on time in terms of a scale factor relative to a_0 , corresponding to a characteristic time at which non-linear structures start to develop in a simulation. For any cosmology (e.g., both EdS and LCDM-like), it can be defined as given by Equation 9, which simply relates it to the value of the variance at a given scale (in this case the mean particle separation Λ in a simulation). Thus, the mapping between EdS and LCDM time evolution is just a function of the mean interparticle spacing Λ and the linear power spectrum of the model, as these allow the determination of a_0 .

Figure A1 illustrates how the parameter $\log_2(a/a_0)$ maps to the redshift in a simulation of a standard LCDM model (“Planck 2013”, Planck Collaboration et al. (2014)). This means that, given a simulation of a determined grid spacing Λ , one can always find a one-to-one relation between the desired evolved redshift of the LCDM and our time variable $\log_2(a/a_0)$. As discussed in Joyce et al. (2021), non-EdS expansion at low redshift introduces the possibility of mapping the time rather than the scale-factor, but the difference in the effective $\log_2(a/a_0)$ is in practice very small, and we will neglect it here.

This mapping allow us to extrapolate the minimum scales from Figure 6, found in EdS cosmologies, into the scales in Figure 7, for a LCDM simulation.

This paper has been typeset from a $\text{\TeX}/\text{\LaTeX}$ file prepared by the author.

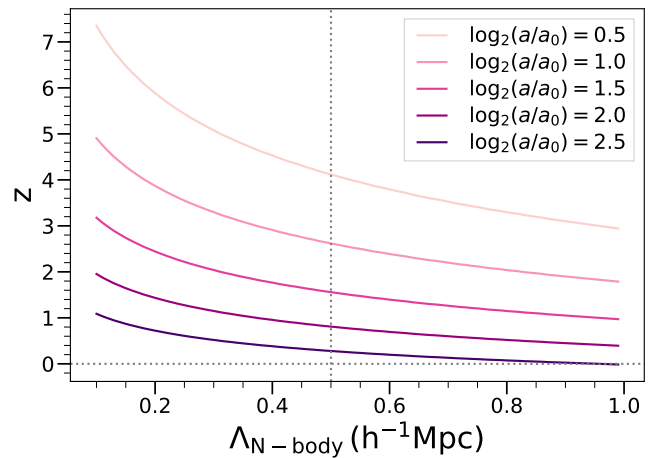


Figure A1. Redshift z corresponding to different fixed values of $\log_2(a/a_0)$ as a function of mean interparticle spacing Λ , using a standard LCDM cosmology (“Planck 2013”, Planck Collaboration et al. (2014)). As discussed in the text, combining this plot with the curves from Figure 6 we can infer a conservative bound on attainable precision as a function of redshift in an LCDM simulation.